

Photocatalytic properties of BiFeO₃ powders synthesized by mixture of CTAB and Glycine

N. Asefi

Iran University of Science and Technology

Masood Hasheminasari (✉ mhashemi@iust.ac.ir)

Iran University of Science and Technology <https://orcid.org/0000-0002-4314-4982>

S. M. Masoudpanah

Iran University of Science and Technology

Research Article

Keywords:

Posted Date: April 8th, 2020

DOI: <https://doi.org/10.21203/rs.3.rs-21520/v1>

License: © ⓘ This work is licensed under a Creative Commons Attribution 4.0 International License.

[Read Full License](#)

Abstract

Highly pure BiFeO₃ (BFO) powders were prepared by solution combustion synthesis method using cetyltrimethylammonium bromide (CTAB) and glycine as fuels at various fuel to oxidant (φ) ratios. Microstructural characteristics, morphology, optical properties, and thermal analysis were studied by X-ray diffraction (XRD), scanning electron microscopy (SEM), diffuse reflectance spectroscopy (DRS), and differential thermal/thermogravimetry (DTA/TGA), respectively. The combusted powders prepared at different fuel content contained some impurity phases such as Bi₂₄Fe₂O₃₉ and Bi₂Fe₄O₉. During the calcination of BFO powders at 600 °C for 1 hour, nearly pure BFO phase was produced. About 80% of methylene blue dye was photodegraded by combusted powders at $\varphi=2$ through 90 minutes of visible light irradiation.

Introduction

Single-phase BiFeO₃ (BFO) is a multiferroic material with distorted rhombohedral and perovskite structure exhibiting the R3c space group. Due to its ferroelectric performance at high Curie temperatures up to 830 °C and antiferromagnetic behavior under its Neel temperature of 370 °C, this material can be considered for the applications in non-volatile memory devices, photovoltaic, sensors and spintronics[1-3].

Because of its narrow bandgap in the range of (2.2 – 2.8 eV) and high chemical stability, BFO has been considered as a visible light photocatalyst to degrade organic pollutants [4]. Many photocatalysts such as TiO₂, ZnO, CdS, ZnS, etc., have been used for the photodegradation of dyes under ultraviolet (UV) light irradiation [5– 10]. However, UV only spans a small portion (~ 4%) of the sunlight spectrum, thus many efforts have been deliberated to develop visible-light catalyst covering a broader spectrum.

Impurity phases such as Bi₂O₃, Bi₂Fe₄O₉, and Bi₂₄Fe₂O₃₉ appear during the synthesis of BFO due to its phase formation's kinetics. Therefore, many researchers developed various synthesis routes to remove these secondary phases, namely through hydrothermal synthesis [11], [12], polymer assisted hydrothermal [13], sol-gel synthesis [14], co-precipitation [15– 17], aerosol-spraying, electrospinning [18], solvothermal route[19], and solution combustion method [20].

Developing simple, environmentally safe, and energy-efficient methods are of great interest to synthesize a pure BFO powder. Solution combustion synthesis (SCS) is a simple, relatively cheap, and fast chemical process to produce various nanomaterials [21]. A self-propagating exothermic reaction takes place between the mixture of metal nitrates and different organic fuels (e.g., glycine, citric acid, urea, etc.), releasing an enormous amount of gaseous products [20].

Among organic fuels, glycine is an amino acid that facilitates the formation of metal ion complex in the solution owing to its carboxylic acid and amino groups at opposite ends of the molecule [22]. BFO has been synthesized by glycine fuel thru microwave-assisted solution combustion with some portion of impurity phases such as Bi₂Fe₄O₉ and Bi₂₄Fe₂O₃₉ [23]. Likewise, Cetyltrimethylammonium bromide

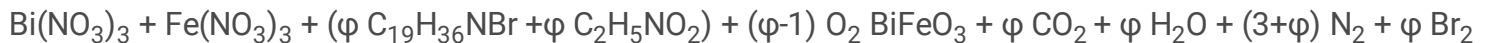
(CTAB) is a cationic surfactant with high decomposition temperature that is extensively used to control particle shapes, size, and microstructure via minimizing the precursor's surface tension [24]. Nevertheless, combining different fuels might be more effectual than that of individual fuels via improved control over the reaction temperature, the type, and the amount of gaseous products released. Therefore, in this project, glycine and CTAB were mixed in the uni-molar ratio to synthesize nearly pure and single-phase BFO.

Experimental Procedure

Synthesis Route

Analytical grades $\text{Fe}(\text{NO}_3)_3 \cdot 9\text{H}_2\text{O}$, $\text{Bi}(\text{NO}_3)_3 \cdot 5\text{H}_2\text{O}$, CTAB $[(\text{C}_{16}\text{H}_{33})\text{N}(\text{CH}_3)_3]\text{Br}$ (> 99%), glycine ($\text{C}_2\text{H}_5\text{NO}_2$), were purchased from Merk Co. without any further purification. Whereby HNO_3 (68 wt %) was added to dissolve bismuth nitrate.

The required amount of $\text{Bi}(\text{NO}_3)_3 \cdot 5\text{H}_2\text{O}$ and $\text{Fe}(\text{NO}_3)_3 \cdot 9\text{H}_2\text{O}$, cetyltrimethylammonium bromide $[(\text{C}_{16}\text{H}_{33})\text{N}(\text{CH}_3)_3]\text{Br}$, and glycine ($\text{C}_2\text{H}_5\text{NO}_2$) were prepared by dissolving 15 mL of 3 mol L^{-1} of HNO_3 in various fuel to oxidant ratios of ($\varphi = 0.5, 0.75, 1$ and 2). H_2O , CO_2 , Br_2 , and N_2 are assumed to be the gaseous products of combustion reaction where the type of gaseous products and adiabatic temperature are controlled by the fuel to oxidant ratio (φ).



IR spectra in the range of ($400-4000 \text{ cm}^{-1}$) were recorded by 8500S SHIMADZU spectrophotometer. Differential thermal (DTA) and thermogravimetry analysis (TGA) were used to study the combustion behavior in the air with a heating rate of $5 \text{ }^\circ\text{C}/\text{min}$ on an STA Ba[®]HR 503 instrument.

Microstructure and phase evolution were examined by X-ray diffraction (PANalytical X'pert, $\text{CuK}\alpha = 1.54060 \text{ \AA}$). Crystallite sizes were also calculated using the raw data from XRD by the Williamson-Hall method.

Field emission scanning electron microscopy (FE-SEM) was acquired to characterize the morphology of the as-combusted powders by TESCAN Vega II.

UV-Vis diffuse reflectance spectrum (DRS) was acquired to measure the bandgap and visible light absorption of the powders by a Shimadzu UV-Vis 52550 spectrophotometer in the wavelength range of ($300-800 \text{ nm}$).

Photocatalytic Performance

Visible light irradiation (two 100 W Xenon lamps with a cutoff ultraviolet filter) was utilized to photodegrade the methylene blue (MB) dye in the presence of as-combusted BFO powders. 100 mg of

BFO catalyst was dispersed in 100 mL of methylene blue (15 mg/L) in the presence of 0.1 mL H₂O₂ (30%) stirred for 60 minutes in dark to obtain the adsorption/desorption equilibrium. Furthermore, the pH of the solution was adjusted by HCl (37 wt%). BFO powders were separated by centrifugation at 6000 rpm for 10 min followed by the MB concentration monitoring on PG Instruments Ltd T80-UV/Vis spectrophotometer.

Results And Discussion

Fig. 1 illustrates the thermal analysis of dried gel produced by a mixture of glycine and CTAB fuels at $\varphi = 1$. A slight drop (~9 %) in the gel's mass is possibly due to the evaporation of absorbed water, while a sharp decline at about 178 °C can be triggered by the exothermic reaction between metal nitrates with glycine and CTAB fuels. This enormous drop (~ 70%) in the mass of gel is because of a combustion reaction that released a large amount of gaseous products such as CO₂, H₂O, N₂, Br₂, etc.

Based on previous findings [25-26], Glycine has a lower decomposition temperature compared to CTAB with fast combustion reaction rate showing sharp weight loss in the gel. Similarly, when the mixture of glycine and CTAB are used as fuels, huge weight loss seems to be dominated by the presence of glycine rather than CTAB. Furthermore, smaller exothermic peak at 285 °C with a gradual weight loss might be attributed to the slow oxidation reaction of residual organics remained in the gel [27].

FTIR spectra of dried gel and as-combusted powders prepared by the mixture of glycine and CTAB fuels at $\varphi = 1$ are illustrated in Fig.2. The broad vibrational stretching modes at the range of 3200-3700 cm⁻¹ correspond to the absorption of hydroxyl groups of water molecules that are omitted in the as combusted BFO powders [28]. Stretching vibration of C-H bonds in CTAB molecules can lead to the formation of bands at 2920 and 2850 cm⁻¹ [29]. The vibrational band at 1350 cm⁻¹ is due to the attachment of CO₂ groups to the cations [28]. The adsorption bands at 1650 cm⁻¹, 1360 cm⁻¹, 902 cm⁻¹, 802 cm⁻¹, and 730 cm⁻¹ confirm the formation of NO⁻³ connected to the CTAB and glycine molecules in the dried gel [30]. Stretching bands at 1757 cm⁻¹ and 1556 cm⁻¹ resemble the existence of COO⁻ groups formed through the oxidation of CTAB molecules [31]. Peaks at 1105 cm⁻¹ and 1020 cm⁻¹ confirm the presence of NH₂ groups. Carboxylate groups can chelate cations leading to the absorption band at 586 cm⁻¹ corresponded to metal-oxygen bonds [32]. Strong peaks at 557 cm⁻¹ and 465 cm⁻¹ of combusted powder can be assigned to the vibrational bending and stretching of Fe-O in the octahedral FeO₆ groups in perovskite structure [33].

XRD patterns of conventionally combusted BFO powders at the various φ values are depicted in Fig. 3. The as combusted powders at $\varphi = 0.5$ and $\varphi = 0.75$ are semi-amorphous, due to their incomplete combustion reaction and low adiabatic combustion temperature. Bi₂Fe₄O₉ (JCDPS Card No. 00-020-0836) impurity phase is presented at φ values of 0.5 and 0.75. However, maximum adiabatic temperature occurs at $\varphi = 1$ leading to a well crystalline pattern. Bi₂₄Fe₂O₃₉ (JCDPS Card No. 00-042-0201) was the only impurity phase formed at the φ values of 1 and 2.

Bi_2O_3 and Fe_2O_3 , as the transitional phases, can take part in the solid reaction of ($\text{Bi}_2\text{O}_3 + \text{Fe}_2\text{O}_3 \rightarrow 2 \text{BiFeO}_3$) to produce the BiFeO_3 phase. Nevertheless, the formation of impurity phases such as $\text{Bi}_2\text{Fe}_4\text{O}_9$ and $\text{Bi}_{24}\text{Fe}_2\text{O}_{39}$ can be ascribed to the insufficiency of Bi_2O_3 and Fe_2O_3 phases initiated by the phase segregation [34]:



Inferior crystallinity of as-combusted powders due to their lower combustion temperatures can be improved by further calcination at higher temperatures (Fig. 4). Impurity phases were mostly eliminated by one-hour calcination at 600 °C due to the reaction of the residual Bi_2O_3 and Fe_2O_3 phases.



SEM micrographs of BFO powders synthesized at different φ values are illustrated in Fig. 5. As combusted powders display a bulky microstructure where the particle sizes are reduced from 37 to 18 nm with the increase in fuel content presented in Table 1, as calculated from XRD data using the Williamson-Hall technique. Particle size mainly depends on the combustion temperature and reaction rate, where the combustion rate would influence the number of nucleation sites and higher combustion temperature enhances the particle growth [35]. When the fuel content is increased, the higher amount of generated heat is consumed by the combustion gases and hence reduces the adiabatic temperature. This decline in the adiabatic temperature resulted in particle size refinement. However, as calcined powders show the particle size enlargement due to the increase in temperature, as depicted in Fig. 5 (d-f).

Another proposed reason behind this particle size refinement at higher CTAB/glycine content, as illustrated schematically in Fig. 6, could be due to the interaction of CTAB micelles with the cationic head inside the solution precursor, separated a large amount of the cationic ends apart and produced smaller BFO nanoparticles when the CTAB amount was maximized. Fig. 7a displays diffuse reflectance spectra of the as combusted BFO powders. The amount of visible light absorption mainly depends on the crystallinity, strain, particle size, impurity phases, and etc. The crystal field and metal-metal transitions highly affect the absorption spectra [36]. The increase in light absorption at higher fuel content ($\varphi=2$), is possibly due to the decrease in the amount of impurity phase $\text{Bi}_{24}\text{Fe}_2\text{O}_{39}$. However, powders synthesized at fuel content of ($\varphi=0.75$) significantly absorbed a higher amount of visible light probably due to the formation of dissimilar impurity phase of $\text{Bi}_2\text{Fe}_4\text{O}_9$, as previously discussed in XRD data. Bandgap energy of the combusted powders was measured by the Tauc's plot ($(\text{ah}\nu)^2$ vs. $\text{h}\nu$), as shown in Fig. 7b and summarized in Table 1. The bandgap energies of the combusted BFO powders are in the range of 1.85-1.96 eV in a good agreement with the bandgap of powders and thin films reported in the literature [36]. At higher fuel contents, the decrease in bandgap energy is mainly due to the particle size refinement

while the increase in the bandgap energy at $\varphi=2$ could be owed to the presence of the impurity phase $\text{Bi}_{24}\text{Fe}_2\text{O}_{39}$.

The relative concentrations (C/C_0) of MB, as an organic pollutant, versus visible light irradiation is illustrated in Fig. 8. The MB is photodegraded by about 80 % during 90 minutes of visible light illumination for combusted powders at φ values of 2 and 0.75. However, the degradation rate is slightly higher for the combusted powders synthesized at $\varphi=2$. Based on our previous findings [23-24], the as combusted powders synthesized by pure glycine or pure CTAB, only showed the photodegradation of MB at about 50 and 30 percents, respectively. Therefore, by mixing the glycine and CTAB fuels, the photodegradation of MB is profoundly enhanced possibly due to the particle size refinement and higher crystallinity with less amount of impurity phases being present. The oxidation and reduction of MB dye molecule to CO_2 and H_2O species mainly depends on the presence of active species such as O^{-2} , OH radicals [37]. The photogenerated electrons and holes during the light absorption of powders would react with the oxygen and water molecules to produce the active species. Thus, the optical properties of combusted powders such as bandgap energy, absorption coefficient, and band edge position play an important role in photocatalytic performance [38].

Conclusions

High purity BFO powders were synthesized via solution combustion synthesis by the mixture of glycine and CTAB as fuels at different fuel contents. The amount of the impurity phase was reduced by increasing fuel content from 0.5 to 2. $\text{Bi}_2\text{Fe}_4\text{O}_9$ impurity phase was present at φ values of 0.5 and 0.75. However, at higher fuel ratios (φ values of 1 and 2) the impurity phase was transformed into the $\text{Bi}_{24}\text{Fe}_2\text{O}_{39}$ phase.

The combusted powders at φ values of 2 and 0.75 showed the highest MB photodegradation of about 80 % under 90 minutes of visible light illumination mainly due to the particle size refinement, higher visible light absorption, and less amount of impurities. Furthermore, the photodegradation rate of combusted powders synthesized at $\varphi=2$ was somewhat enhanced.

References

- [1] H. Shokrollahi, "Magnetic, electrical and structural characterization of BiFeO_3 nanoparticles synthesized by co-precipitation," *Powder Technol.*, vol. 235, pp. 953–958, 2013.
- [2] P. R. Vanga, R. V Mangalaraja, and M. Ashok, "Structural, magnetic and photocatalytic properties of La and alkaline co-doped BiFeO_3 nanoparticles," *Mater. Sci. Semicond. Process.*, vol. 40, pp. 796–802, 2015.
- [3] S. Chen *et al.*, "Hand-Fabricated CNT/AgNps electrodes using Wax-on-plastic platforms for electro-Immuno-sensing Application," *Sci. Rep.*, vol. 9, no. 1, p. 6131, 2019.

- [4] R. Guo, L. Fang, W. Dong, F. Zheng, and M. Shen, "Enhanced photocatalytic activity and ferromagnetism in Gd doped BiFeO₃ nanoparticles," *J. Phys. Chem. C*, vol. 114, no. 49, pp. 21390–21396, 2010.
- [5] Y. Chen, Y. Tang, S. Luo, C. Liu, and Y. Li, "TiO₂ nanotube arrays co-loaded with Au nanoparticles and reduced graphene oxide: Facile synthesis and promising photocatalytic application," *J. Alloys Compd.*, vol. 578, pp. 242–248, 2013.
- [6] Y. Zhang, W. Cui, W. An, L. Liu, Y. Liang, and Y. Zhu, "Combination of photoelectrocatalysis and adsorption for removal of bisphenol A over TiO₂-graphene hydrogel with 3D network structure," *Appl. Catal. B Environ.*, vol. 221, pp. 36–46, 2018.
- [7] A. Nag, S. Sapra, S. Chakraborty, S. Basu, and D. D. Sarma, "Synthesis of CdSe nanocrystals in a noncoordinating solvent: effect of reaction temperature on size and optical properties," *J. Nanosci. Nanotechnol.*, vol. 7, no. 6, pp. 1965–1968, 2007.
- [8] K. Rajeshwar *et al.*, "Heterogeneous photocatalytic treatment of organic dyes in air and aqueous media," *J. Photochem. Photobiol. C Photochem. Rev.*, vol. 9, no. 4, pp. 171–192, 2008.
- [9] J.-M. Herrmann, "Heterogeneous photocatalysis: fundamentals and applications to the removal of various types of aqueous pollutants," *Catal. today*, vol. 53, no. 1, pp. 115–129, 1999.
- [10] Y. Fu and X. Wang, "Magnetically separable ZnFe₂O₄-graphene catalyst and its high photocatalytic performance under visible light irradiation," *Ind. Eng. Chem. Res.*, vol. 50, no. 12, pp. 7210–7218, 2011.
- [11] T. Gao *et al.*, "Shape-controlled preparation of bismuth ferrite by hydrothermal method and their visible-light degradation properties," *J. Alloys Compd.*, vol. 648, pp. 564–570, 2015.
- [12] X. Wang *et al.*, "PVP assisted hydrothermal fabrication and morphology-controllable fabrication of BiFeO₃ uniform nanostructures with enhanced photocatalytic activities," *J. Alloys Compd.*, vol. 677, pp. 288–293, 2016.
- [13] Y. Wang *et al.*, "Low temperature polymer assisted hydrothermal synthesis of bismuth ferrite nanoparticles," *Ceram. Int.*, vol. 34, no. 6, pp. 1569–1571, 2008.
- [14] T. Gao *et al.*, "Synthesis of BiFeO₃ nanoparticles for the visible-light induced photocatalytic property," *Mater. Res. Bull.*, vol. 59, pp. 6–12, 2014.
- [15] H. Ke *et al.*, "Factors controlling pure-phase multiferroic BiFeO₃ powders synthesized by chemical co-precipitation," *J. Alloys Compd.*, vol. 509, no. 5, pp. 2192–2197, 2011.
- [16] H. Y. Bo, G. Q. Tan, H. Y. Miao, and A. Xia, "Co-precipitation synthesis of BiFeO₃ powders," in *Advanced Materials Research*, 2010, vol. 105, pp. 286–288.

- [17] Z. Liu, Y. Qi, and C. Lu, "High efficient ultraviolet photocatalytic activity of BiFeO₃ nanoparticles synthesized by a chemical coprecipitation process," *J. Mater. Sci. Mater. Electron.*, vol. 21, no. 4, pp. 380–384, 2010.
- [18] W. Wang *et al.*, "Electrospinning of magnetical bismuth ferrite nanofibers with photocatalytic activity," *Ceram. Int.*, vol. 39, no. 4, pp. 3511–3518, 2013.
- [19] Y. Huo, Y. Jin, and Y. Zhang, "Citric acid assisted solvothermal synthesis of BiFeO₃ microspheres with high visible-light photocatalytic activity," *J. Mol. Catal. A Chem.*, vol. 331, no. 1–2, pp. 15–20, 2010.
- [20] J. Yang, X. Li, J. Zhou, Y. Tang, Y. Zhang, and Y. Li, "Factors controlling pure-phase magnetic BiFeO₃ powders synthesized by solution combustion synthesis," *J. Alloys Compd.*, vol. 509, no. 37, pp. 9271–9277, 2011.
- [21] S. T. Aruna and A. S. Mukasyan, "Combustion synthesis and nanomaterials," *Curr. Opin. solid state Mater. Sci.*, vol. 12, no. 3–4, pp. 44–50, 2008.
- [22] A. Motevalian and S. Salem, "Effect of glycine–starch mixing ratio on the structural characteristics of MgAl₂O₄ nano-particles synthesized by sol–gel combustion," *Particuology*, vol. 24, pp. 108–112, 2016.
- [23] N. Asefi, S. M. Masoudpanah, and M. Hasheminasari, "Microwave-assisted solution combustion synthesis of BiFeO₃ powders," *J. Sol-Gel Sci. Technol.*, pp. 1–9, 2018.
- [24] N. Asefi, M. Hasheminasari, and S. M. Masoudpanah, "Solution Combustion Synthesis of BiFeO₃ Powders Using CTAB as Fuel," *J. Electron. Mater.*, pp. 1–7, 2018.
- [25] J. Huang, G. Tan, W. Yang, L. Zhang, H. Ren, and A. Xia, "Microwave hydrothermal synthesis of BiFeO₃: impact of different surfactants on the morphology and photocatalytic properties," *Mater. Sci. Semicond. Process.*, vol. 25, pp. 84–88, 2014.
- [26] U. A. Joshi, J. S. Jang, P. H. Borse, and J. S. Lee, "Microwave synthesis of single-crystalline perovskite Bi Fe O₃ nanocubes for photoelectrode and photocatalytic applications," *Appl. Phys. Lett.*, vol. 92, no. 24, p. 242106, 2008.
- [27] M. Radpour, S. M. Masoudpanah, and S. Alamolhoda, "Microwave-assisted solution combustion synthesis of Fe₃O₄ powders," *Ceram. Int.*, vol. 43, no. 17, pp. 14756–14762, 2017.
- [28] G. Socrates, "Infrared and Raman Characteristic Group Frequencies, 3rd edn., J." Wiley & Sons Ltd., England, 2001.
- [29] S. F. N. Hamedani, S. M. Masoudpanah, M. S. Bafghi, and N. A. Baloochi, "Solution combustion synthesis of CoFe₂O₄ powders using mixture of CTAB and glycine fuels," *J. Sol-Gel Sci. Technol.*, vol. 86, no. 3, pp. 743–750, 2018.

- [30] P. Naderi, S. M. Masoudpanah, and S. Alamolhoda, "Magnetic properties of $\text{Li}_0.5\text{Fe}_2\text{O}_4$ nanoparticles synthesized by solution combustion method," *Appl. Phys. A*, vol. 123, no. 11, p. 702, 2017.
- [31] S. Shabani, S. M. Mirkazemi, S. M. Masoudpanah, and P. T. D. Abadi, "Synthesis and characterization of pure single phase BiFeO_3 nanoparticles by the glyoxylate precursor method," *J. Supercond. Nov. Magn.*, vol. 27, no. 12, pp. 2795–2801, 2014.
- [32] J. L. Ortiz-Quiñonez *et al.*, "Easy synthesis of high-purity BiFeO_3 nanoparticles: new insights derived from the structural, optical, and magnetic characterization," *Inorg. Chem.*, vol. 52, no. 18, pp. 10306–10317, 2013.
- [33] S. M. Masoudpanah, S. M. Mirkazemi, R. Bagheriyeh, F. Jabbari, and F. Bayat, "Structural, magnetic and photocatalytic characterization of $\text{Bi}_{1-x}\text{La}_x\text{FeO}_3$ nanoparticles synthesized by thermal decomposition method," *Bull. Mater. Sci.*, vol. 40, no. 1, pp. 93–100, 2017.
- [34] K. Feng, L.-C. Wang, J. Lu, Y. Wu, and B.-G. Shen, "Experimentally determining the intrinsic center point of $\text{Bi}_2\text{O}_3\text{-Fe}_2\text{O}_3$ phase diagram for growing pure BiFeO_3 crystals," *CrystEngComm*, vol. 15, no. 24, pp. 4900–4904, 2013.
- [35] F. Deganello and A. K. Tyagi, "Solution combustion synthesis, energy and environment: Best parameters for better materials," *Prog. Cryst. Growth Charact. Mater.*, vol. 64, no. 2, pp. 23–61, 2018.
- [36] S.-M. Lam, J.-C. Sin, and A. R. Mohamed, "A newly emerging visible light-responsive BiFeO_3 perovskite for photocatalytic applications: A mini review," *Mater. Res. Bull.*, vol. 90, pp. 15–30, 2017.
- [37] K. Prashanthi, G. Thakur, and T. Thundat, "Surface enhanced strong visible photoluminescence from one-dimensional multiferroic BiFeO_3 nanostructures," *Surf. Sci.*, vol. 606, no. 19–20, pp. L83–L86, 2012.
- [38] T. Soltani and M. H. Entezari, "Photolysis and photocatalysis of methylene blue by ferrite bismuth nanoparticles under sunlight irradiation," *J. Mol. Catal. A Chem.*, vol. 377, pp. 197–203, 2013.

Table

Table 1 Crystallite size (D_{XRD}) of BiFeO_3 phase, and bandgap energy (E_g) as a function of fuel type.

As-combusted	D_{XRD} (nm)	E_g (eV)
0.5	37	1.96
0.75	28	1.85
1	21	1.96
2	18	1.96

Figures

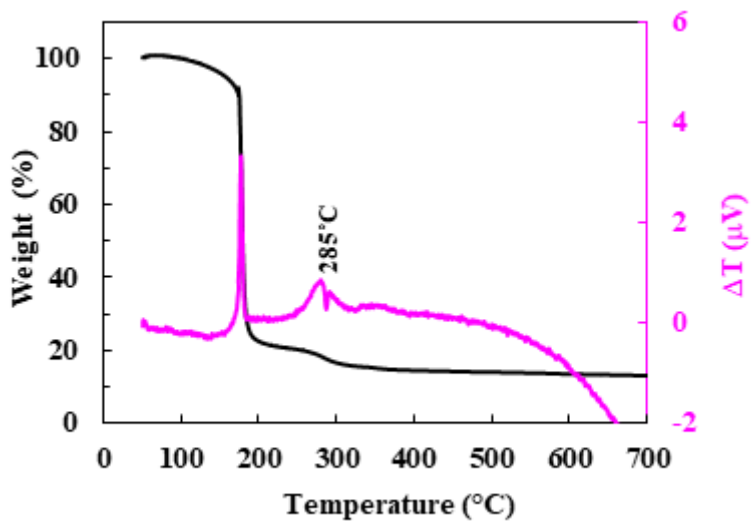


Figure 2

TGA/DTA curves of the dried gel prepared by a mixture of CTAB and glycine fuels at $\phi = 1$.

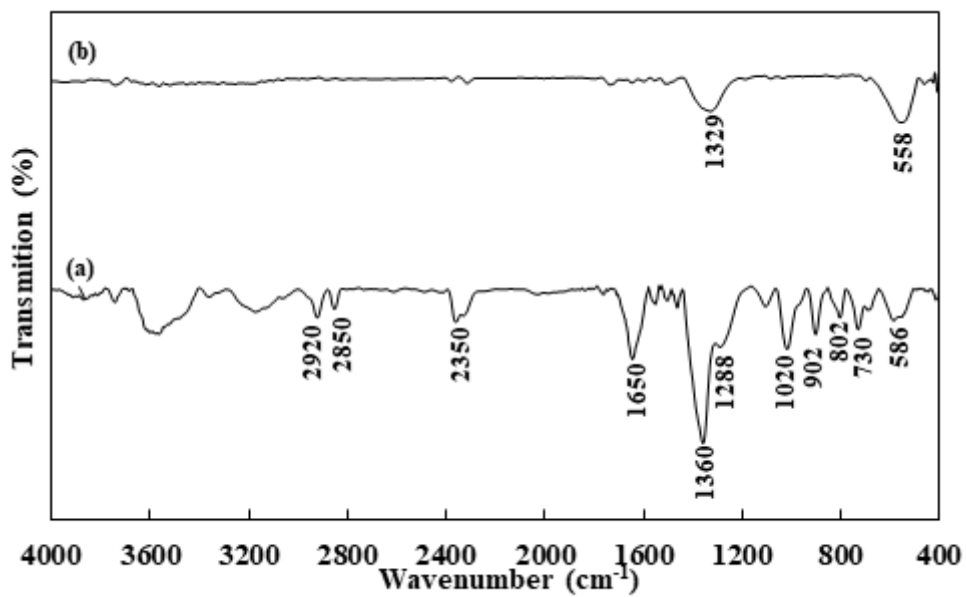


Figure 4

FTIR spectra of (a) dried gel and (b) the as-combusted BFO powders at $\phi = 1$.

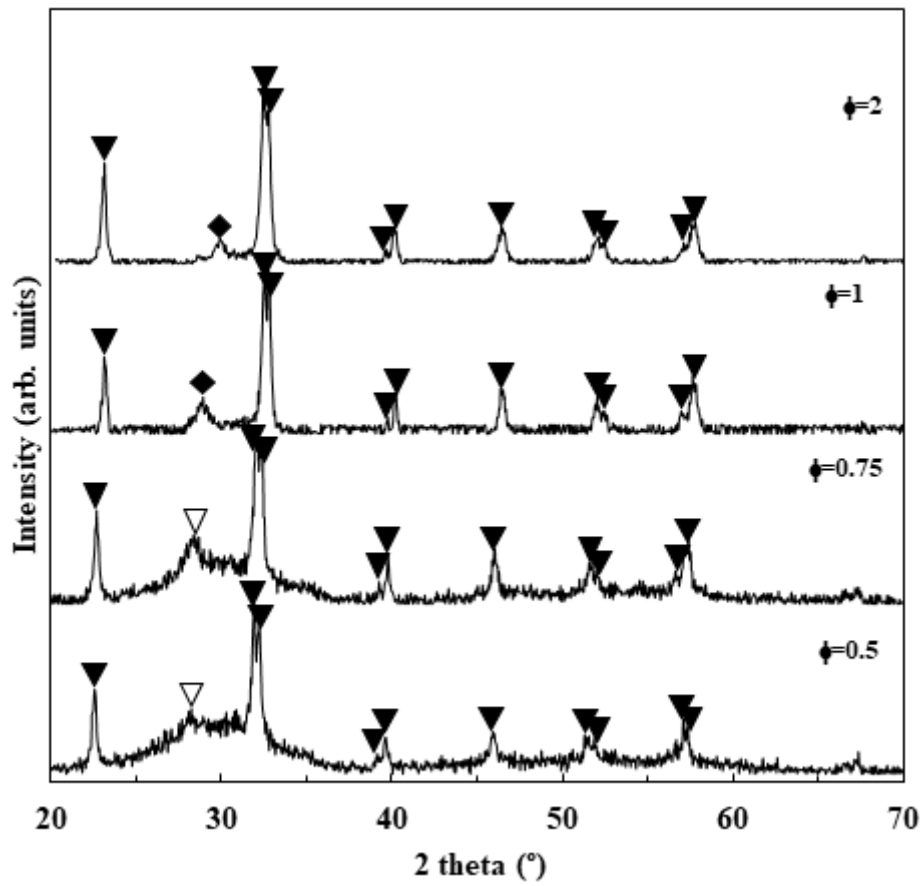


Figure 6

XRD patterns of the as-combusted BFO powders using glycine and CTAB fuel content. (▲ : BiFeO₃, ◆ : Bi₂Fe₄O₉, △ : Bi₂₄Fe₂₀O₃₉)

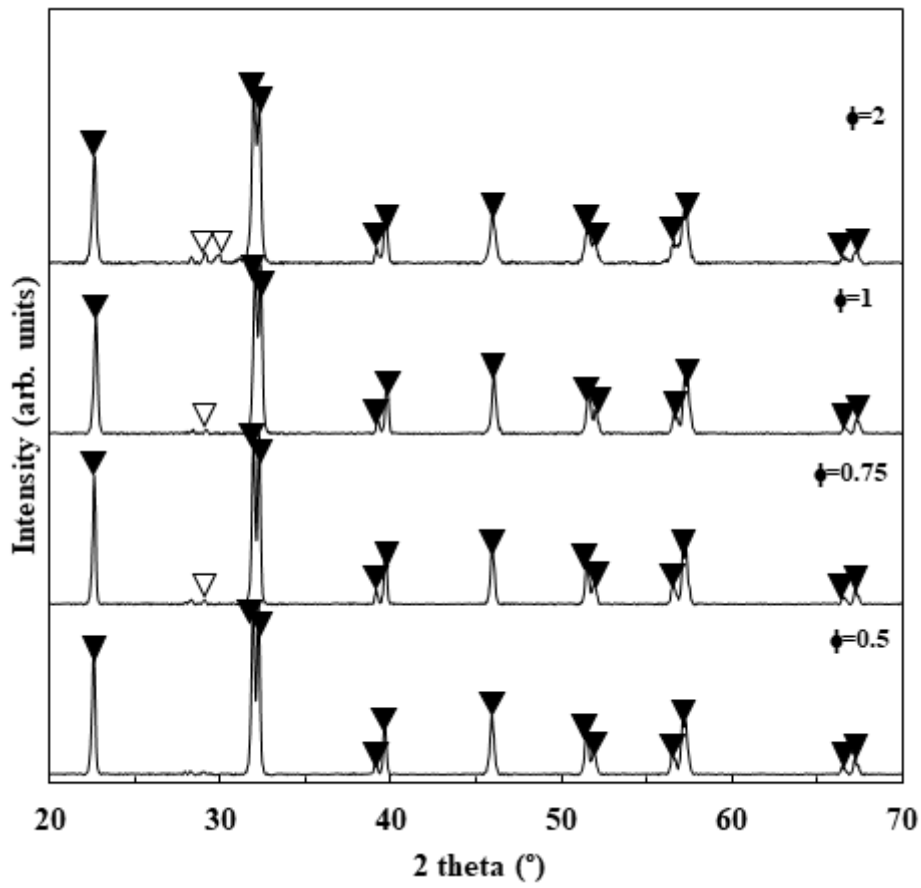


Figure 8

XRD patterns of the as-calcined BFO powders using glycine and CTAB fuel content. (: BiFeO₃, : Bi₂Fe₄O₉).

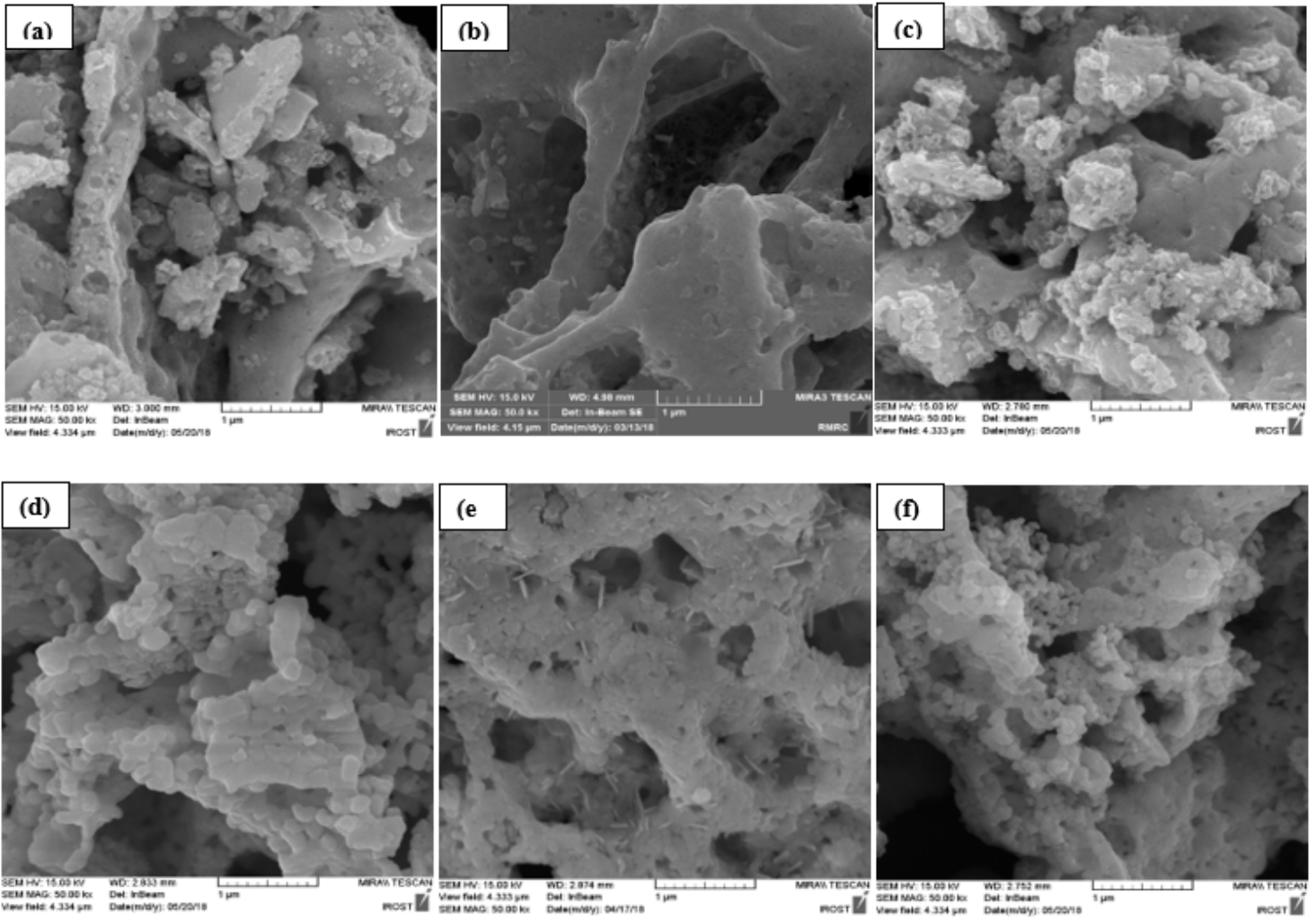


Figure 10

SEM micrographs of the as-combusted BFO powders at (a) $\phi = 0.75$, (b) $\phi = 1$ and (c) $\phi = 2$ and the as-calcined BFO powders at (d) $\phi = 0.75$, (e) $\phi = 1$ and (f) $\phi = 2$.

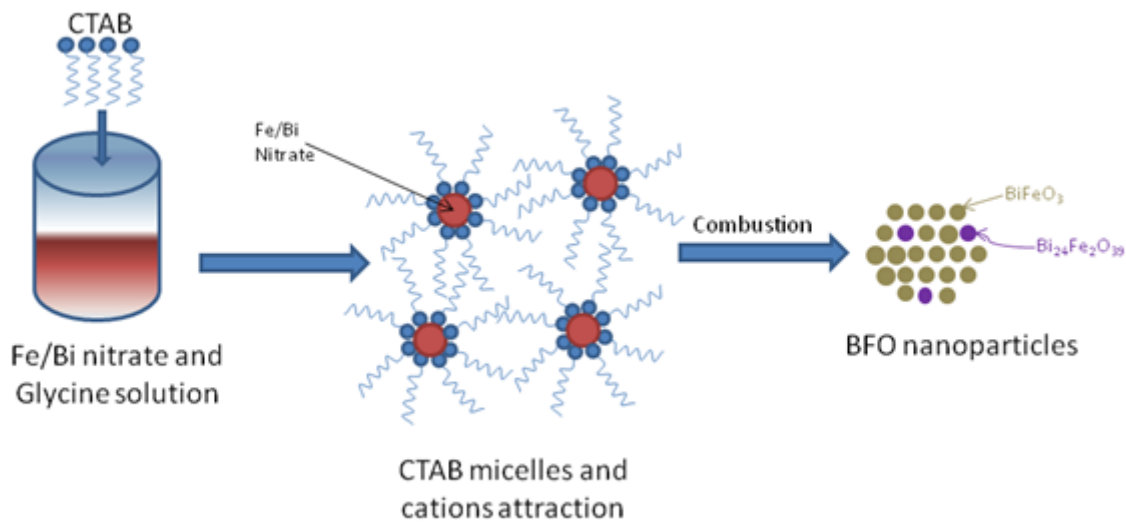


Figure 12

Schematic of BFO nanoparticle synthesis via micells formation at high CTAB content.

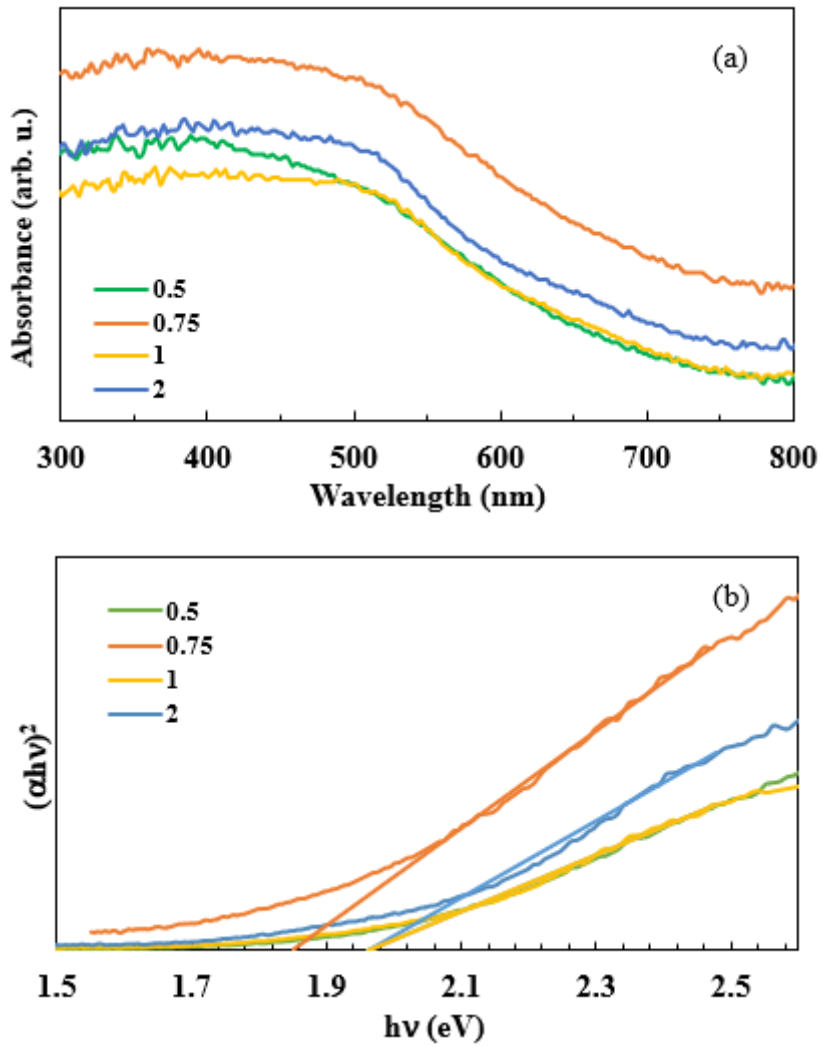


Figure 14

(a) UV-Vis diffuse reflectance spectra and (b) Tauc's plot of the as-combusted BFO powders.

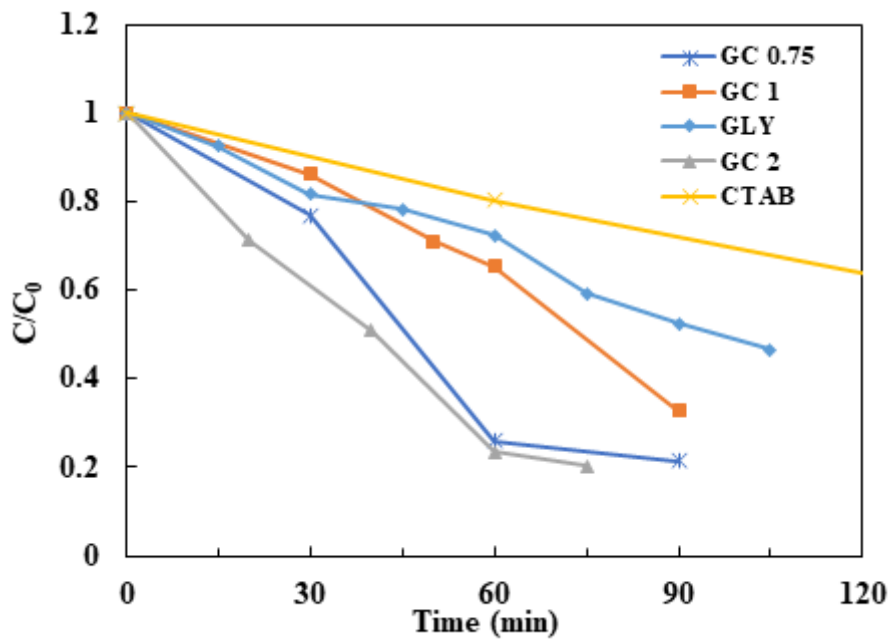


Figure 16

C/C0 vs. irradiation time in the presence of the BFO powders at different fuel content and type.